Defect engineering of 1T' MX 2 (M = Mo, W and X = S, Se) transition metal dichalcogenide-based electrocatalyst for alkaline hydrogen evolution reaction

Samuel Akinlolu Ogunkunle, Assil Bouzid, Jack Jon Hinsch, Oscar Allen, Jessica Jein White, Samuel Bernard, Zhenzhen Wu, Yong Zhu, Yun Wang

Journal of Physics:
Condensed Matter

PAPER • **OPEN ACCESS**

Defect engineering of 1T′ MX_2 (M = Mo, W and X = S, Se) transition metal dichalcogenide-based electrocatalyst for alkaline hydrogen evolution reaction

To cite this article: Samuel Akinlolu Ogunkunle *et al* 2024 *J. Phys.: Condens. Matter* **36** 145002

OPEN ACCESS
IOP Publishing
Journal of Physics: Condensed Matter
J. Phys.: Condens. Matter **36** (2024) 145002 (8pp)
https://doi.org/10.1088/1361-648X/ad19a4

Defect engineering of 1T′ MX_2 (M = Mo, W and X = S, Se) transition metal dichalcogenide-based electrocatalyst for alkaline hydrogen evolution reaction

Samuel Akinlolu Ogunkunle[1], Assil Bouzid[2], Jack Jon Hinsch[1], Oscar J Allen[1], Jessica Jein White[1], Samuel Bernard[2], Zhenzhen Wu[1], Yong Zhu[3] and Yun Wang[1,*]

[1] Centre for Clean Environment and Energy, School of Environment and Science, Griffith University, Gold Coast Campus, Southport 4222, Australia
[2] Institut de Recherche sur les Céramiques (IRCER), UMR CNRS 7315-Université de Limoges, Limoges 87068, France
[3] School of Engineering and Built Environment, Griffith University, Gold Coast Campus, Southport 4222, Australia

E-mail: yun.wang@griffith.edu.au

Received 18 September 2023, revised 28 November 2023
Accepted for publication 28 December 2023
Published 5 January 2024

Abstract

The alkaline electrolyzer (AEL) is a promising device for green hydrogen production. However, their energy conversion efficiency is currently limited by the low performance of the electrocatalysts for the hydrogen evolution reaction (HER). As such, the electrocatalyst design for the high-performance HER becomes essential for the advancement of AELs. In this work, we used both hydrogen (H) and hydroxyl (OH) adsorption Gibbs free energy changes as the descriptors to investigate the catalytic HER performance of 1T′ transition metal dichalcogenides (TMDs) in an alkaline solution. Our results reveal that the pristine sulfides showed better alkaline HER performance than their selenide counterparts. However, the activities of all pristine 1T′ TMDs are too low to dissociate water. To improve the performance of these materials, defect engineering techniques were used to design TMD-based electrocatalysts for effective HER activity. Our density functional theory results demonstrate that introducing single S/Se vacancy defects can improve the reactivities of TMD materials. Yet, the desorption of OH becomes the rate-determining step. Doping defective MoS_2 with late 3d transition metal (TM) atoms, especially Cu, Ni, and Co, can regulate the reactivity of active sites for optimal OH desorption. As a result, the TM-doped defective 1T′ MoS_2 can significantly enhance the alkaline HER performance. These findings highlight the potential of defect engineering technologies for the design of TMD-based alkaline HER electrocatalysts.

* Author to whom any correspondence should be addressed.

Supplementary material for this article is available online

Keywords: alkaline hydrogen evolution reaction, defect engineering, transition metal dichalcogenide, density functional theory, descriptor

1. Introduction

Green hydrogen can be produced through water electrolysis using electricity from renewable sources like solar and wind, which is considered as a promising solution compared to 'gray' hydrogen generated from steam methane reforming, contributing to CO and CO_2 emissions [1]. The cost of green hydrogen production is influenced by the expense of renewable electricity and the energy efficiency of water electrolyzers [1]. The hydrogen evolution reaction (HER) via water splitting can occur either in acidic or alkaline environments [2]. While acidic solutions are more efficient due to the high concentration of H+ ions and the availability of commercial proton membranes, HER electrocatalysts, such as Pt, are costly and rare [3]. On the other hand, the industrial utilization of alkaline media for large-scale hydrogen production is more popular due to the use of earth-abundant catalysts [4, 5]. Despite technological advancements, the energy conversion efficiency of market-leading alkaline electrolyzers (AELs) remains relatively low, which calls for the design of new high-performance alkaline HER electrocatalysts.

Recent studies have shown promising results regarding TMDs as HER catalysts [6–11]. The metallic 1T or 1T′ TMDs show promise for HER due to their electronic structure, high conductivity, tunable properties, and active catalytic sites [12–17]. Previous computational studies mainly focused on the H adsorption-free energy (ΔG_{H^*}) as a descriptor for 1T-TMDs in HER [6, 18, 19]. This is because the HER in acidic media begins with the discharge of a proton (Volmer reaction, equation (1)) and can proceed through either the electrodesorption step (Heyrovsky reaction, equation (2)) or the proton recombination step (Tafel reaction, equation (3))

$$\text{Volmer reaction: } H^+ + e^- \rightarrow H^* \quad (1)$$

$$\text{Heyrovsky reaction: } H^* + H^+ + e^- \rightarrow H_2 \quad (2)$$

$$\text{Tafel reaction: } H^* + H^* \rightarrow H_2. \quad (3)$$

Under alkaline conditions, the Volmer and Heyrovsky reactions differ due to the presence of hydroxide ions (OH^-). The Volmer reaction (equation (4)) involves the electrochemical reduction of water (H_2O) to form an adsorbed hydrogen species (H^*) and hydroxide ions. The Heyrovsky reaction (equation (5)) occurs when the adsorbed hydrogen species reacts with a proton, electron, and hydroxide ion to produce molecular hydrogen and hydroxide ions. The Tafel reaction (equation (6)) remains unchanged, representing the interaction between two adsorbed hydrogen species to form H_2

$$\text{Volmer reaction: } H_2O + e^- \rightarrow H^* + OH^- \quad (4)$$

$$\text{Heyrovsky reaction: } H_2O + e^- + H^* \rightarrow H_2 + OH^- \quad (5)$$

$$\text{Tafel reaction: } H^* + H^{+*} \rightarrow H_2. \quad (6)$$

Consequently, breaking the covalent H–OH bond in the Volmer reaction becomes essential in an alkaline solution. This has led to a debate in the literature challenging the traditional approach of using the Gibbs free energy change of the hydrogen adsorption as the sole reaction descriptor for HER in favor of considering the complex phenomenological approach of the alkaline environment [20]. In alkaline media, the adsorption of OH intermediate, which is proportional to the H–OH bond dissociation barrier according to the Brønsted–Evans–Polanyi relationship is equally important [21]. To this end, the Gibbs free energy change of OH adsorption (ΔG_{HO^*}) can be considered another critical descriptor for alkaline HER. Previous studies on Pt-based electrocatalysts demonstrated that the desired values for ΔG_{H^*} and ΔG_{OH^*} are 0.0 eV and −0.3 eV, respectively [21]. To our knowledge, no theoretical study has focused on TMDs for electrocatalytic HER in alkaline solutions by using both ΔG_{H^*} and ΔG_{OH^*} as descriptors.

In this study, we resort to the density functional theory (DFT) method to calculate both ΔG_{H^*} and ΔG_{OH^*} values of several TMD-based materials and assess the performance of these materials in alkaline HER. The DFT results demonstrate that defect engineering is a promising root for developing efficient TMD-based HER electrocatalysts in an alkaline solution.

2. Computational details

The Vienna *Ab-initio* Simulation Package was employed to perform spin-polarized DFT calculations [22–25]. To account for electron exchange and correlation effects, the Perdew–Burke–Ernzerhof (PBE) functional based on a generalized gradient approximation was chosen [22, 26]. The electron–ion interaction was described using the projector-augmented wave method [27]. The valence configuration for Mo, W, Fe, Co, Ni, S, Se, O, and H are $4s^2 4p^6 5s^1 4d^5$ for $5s^2 5p^6 6s^1 5d^5$, $3d^6 4s^2$, $3d^7 4s^2$, $3d^8 4s^2$, $3s^2 3p^4$, $4s^2 4p^4$, $2s^2 2p^4$ and $1s^1$ respectively. The cut-off energy of the plane wave was set to 520 eV. Since traditional DFT calculations at the PBE level cannot correctly include the nonlocal van der Waals interactions, the calculations with dispersion corrections may affect the adsorption energies of small molecules [28]. In this regard, the DFT-D3 method was adopted for dispersion corrections here [28]. Due to the large Coulombic repulsion between localized d electrons of transition metals (TMs), the DFT + U method was used to

correct the material properties of TM oxides, particularly for magnetic ground states and electronic structures. For Ti, V, Cr, Mn, Fe, Co and Ni, U–J values are set as 4.3, 3.4, 3.2, 3.5, 4.3, 4.0, 5.5 eV, respectively, which have been justified in our recent studies [29–32]. A vacuum region of 25 Å was used to avoid interaction between slabs. All calculations used a (1×2) 1T′ TMD monolayer, which has the same size of the (2×2) cell of the high-symmetry 1H TMD monolayer [25, 33]. The 1T′ MX_2 (M = Mo, W and X = S, Se) TMDs were chosen since they have been previously reported to have metallic properties with high electric conductivity [12, 14, 15, 34–37], which can be beneficial to the charge transfer and leads to an improved electrocatalysis performance. During the geometry optimization, all the atoms were relaxed with energy and force convergence smaller than 1×10^{-5} eV and 1×10^{-2} eV Å^{-1}, respectively.

The ΔG_{H^*} was computed from the following equation:

$$\Delta G_{H^*} = \Delta E_{H^*} + T\Delta S + \Delta ZPE \tag{7}$$

where ΔE_{H^*} is the adsorption energy of H atoms, which can be calculated from the following equations

$$\Delta E_{H^*} = E_{H^*} - E_* - \frac{1}{2}E_{H_2} \tag{8}$$

where E_{H^*} and E_* are the energies of the TMD monolayers with and without absorbed H atoms, respectively. T, ΔS, and ΔZPE in equation (7) are the room temperature (T = 298.15 K), entropy change, and zero-point energy change, respectively, which values are obtained from the literature [22, 26, 38]. Accordingly, the ΔG_{OH^*} was computed as follows:

$$\Delta G_{OH^*} = \Delta E_{OH^*} + T\Delta S + \Delta ZPE. \tag{9}$$

The adsorption energy of OH was calculated as follows:

$$\Delta E_{OH^*} = \left(E_{OH^*} - E_* + E_{H_2O} + \frac{1}{2}E_{H_2} - 2E_{H_2O}\right) \tag{10}$$

E_{OH^*} is the energies of the monolayer with adsorbed OH, and E_{H_2O} is the energy of an isolated water molecule.

3. Results and discussion

3.1. Pristine 1T′ MX_2 (M = Mo, W and X = S, Se) TMD

The ΔG_{H^*} and ΔG_{OH^*} were first used as the descriptors to evaluate the alkaline HER performance of pristine 1T′ MX_2 (M = Mo, W and X = S, Se) TMD, which atomic structure was illustrated in figure 1(a). Due to the low symmetry of 1T′ phase of TMDs, some X atoms are higher (termed as High X) than the rest (termed as Low X) in the top layer. Both figures 1(b) and (c) show the adsorption of hydrogen atom intermediates on High X atoms and Low X, respectively. The OH intermediate was adsorbed at the top of the metal of the MX_2 monolayer, which is associated with the High and Low X sites. The ΔG_{H^*} and ΔG_{OH^*} values are shown in figure 1(d) and listed in table S1. It can be found that ΔG_{H^*} values of sulfides are lower than that of the selenides, indicating higher reactivity of S for H adsorption compared to Se. This can be understood in terms of the lower S electronegativity, which also agrees with the conclusions of previous studies dealing with $MoSe_2$ and WSe_2 that showed lower HER activity and poor H* adsorption compared to MoS_2 and WS_2 [39, 40]. In general, the stronger adsorption of H on Low X is reflected by the slightly short X–H bond lengths listed in table S1. The stronger adsorption of H on Low X can be ascribed to the weaker interaction between M and Low X, which can be evidenced by the longer bond length between Low X and M [41, 42]. Interestingly, the ΔG_{H^*} values on Low S are close to the desired one of 0.0 eV. It suggests that these 1T′ MoS_2 and WS_2 can be suitable acidic HER electrocatalysts. However, all pristine TMDs considered here have high ΔG_{OH^*} larger than 1.5 eV, far from the ideal value of −0.3 eV [21]. The high ΔG_{OH^*} values indicate that water dissociation becomes the rate-determination step (RDS) for alkaline HER due to the low activity of these TMDs. Thus, their reactivity for water dissociation needs to be further improved to enable a better energy conversion efficiency of 1T′ TMD for alkaline HER electrocatalysis.

3.2. Single X vacancy defective TMD

The occurrence of vacancies in metallic TMDs has been experimentally demonstrated to possess a much higher reactivity [15]. As such, the defective TMDs hold the potential for higher energy conversion efficiency during alkaline HER. Recent studies have revealed that the intrinsic properties of TMDs, such as electronics, optical, mechanical, and thermal properties, can be altered by defects in the TMDs [43–46]. Previous studies considered six kinds of point defects: monochalcogenide vacancy (X vacancy), dichalcogenide vacancy ($2X$ vacancy), aligned dichalcogenide vacancy, and aligned monochalcogenide vacancy ($2X$s vacancy), metal vacancy (M vacancy), vacancy complex of M and three adjacent chalcogens ($MX3$ vacancy), and vacancy complex of M and three adjacent chalcogen pairs ($MX6$ vacancy) [43, 47, 48]. It has been demonstrated that X vacancy is the easiest to form, with the highest abundance in the defective TMDs [43]. In this regard, only X vacancy was considered in this study. The X vacancy can be generated by removing either Low or High X from the pristine TMDs, as shown in figures 2(a) and (b) respectively. For all four kinds of 1T′ TMDs considered in this study, the formation of Low X vacancy is more energetically preferred (see table S2). Consequently, only the Low X vacancy was considered in the remaining part of this work.

The hydrogen can be adsorbed on the top of the Low or High X next to the Low X vacancy, as shown in figure 2(c), respectively. Similarly, the trend observed on the pristine TMD monolayer, the adsorption of H atoms on the Low X is energetically preferred. The single X vacancy defects have considerable impacts on H adsorption. The ΔG_{H^*} values of MoS_2 and WS_2 decrease by 31% and 16%, respectively (see tables S1 and S2). Accordingly, the ΔG_{H^*} values of $MoSe_2$ and WSe_2 reduced by 22% and 17%, respectively (see tables S1 and S2). This observation implies that X vacancies in TMDs

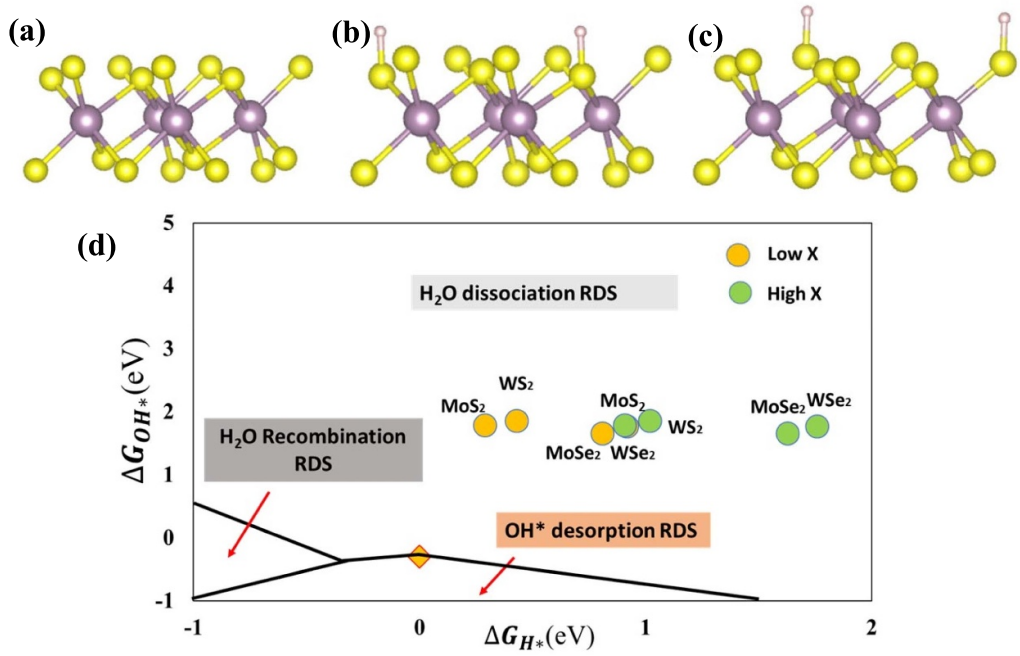

Figure 1. Atomic structure of a typical (a) pristine 1T′ MX_2 TMD; (b) pristine 1T′ MX_2 TMD with hydrogen atom to the High X; (c) pristine 1T′ MX_2 TMD with hydrogen atom to the Low X; and (d) plot of ΔG_{OH^*} against ΔG_{H^*} of MX_2 TMDs. Color code: yellow: X (S or Se), and purple: TM (Mo or W).

can alter their electronic structure and boost their catalytic activity for the HER.

Figure 2(d) shows the adsorption configuration of the intermediate OH on the X vacancy site of 1T′ TMDs. Unlike the H adsorption on the X atoms, where the electronic properties of the X atoms were indirectly affected by the neighboring X vacancy, the OH species directly adsorb at the X vacancy site. Consequently, the impact of X vacancy on the ΔG_{OH^*} is much more significant than that of their corresponding pristine TMDs. The ΔG_{OH^*} values are shown in figure 2(e) and listed in table S2. All the ΔG_{HO^*} values on the X vacancy site are significantly reduced by 165%, 163%, 183%, and 178% for MoS_2, $MoSe_2$, WS_2, and WSe_2, respectively (see tables S1 and S2), which indicates a tremendous improvement in the reactivity of 1T′ TMDs for OH adsorption. It is worth noting that the relative reduction amplitude of ΔG_{OH^*} values is more affected by the metal since the OH is directly associated with the metals. The ΔG_{OH^*} values exhibit a particularly significant decrease more significantly on WX_2. Figure 2(e) displays a volcano plot, illustrating that the ΔG_{OH^*} values are lower than the optimal value of −0.3 eV. The low ΔG_{OH^*} values indicate that the X vacancy sites within all TMD monolayers are too reactive to OH desorption. Consequently, the OH desorption becomes the RDS for alkaline HER. To further improve the TMD-based alkaline HER performance, manipulating the activity of the X vacancy site becomes the critical factor. Since the S vacancy site in the 1T′ MoS_2 monolayer has the highest performance, as evidenced by figure 2(e), the defective 1T′ MoS_2 monolayer was then used as the model system for the further electrocatalyst design.

3.3. 3d TM doped defective MoS_2

Various research studies have aimed to enhance the efficiency of HER catalysts doping with TM dopants [32]. To this end, we purposely incorporate widely used 3d TM such as Ti, V, Cr, Mn, Fe, Co, Ni, Cu, and Zn dopants to defective 1T′ MoS_2 with S vacancy to optimize the adsorption strength of OH and H species on TMDs for alkaline HER. The calculated plot of ΔG_{OH^*} against ΔG_{H^*} is shown in figure 3. Our DFT results demonstrate that ΔG_{H^*} increases after introducing early 3d TM dopants (see table S3) and that it decreases with the introduction of late 3d TM dopants except in the case of Zn-doped MoS_2 (see table S4). Noteworthy, the ΔG_{H^*} values of Fe-, Co-, Ni- and Cu-doped defective 1T′ MoS_2 are close to the optimal ΔG_{H^*} value of 0.0 eV. The ΔG_{H^*} value is often used as the only descriptor to screen the performance of the acidic HER electrocatalyst [32]. Consequently, the S atoms next to the metal dopant and S vacancy are highly favorable for acidic HER.

The ΔG_{HO^*} value is another important indicator for the alkaline HER catalysts' design. The introduction of early 3d TM doping led to a significant change in ΔG_{OH^*} values. Generally, ΔG_{OH^*} values increase with the increase of the atomic number of the 3d TM dopant. The only exceptions are the Fe- and Zn-doped 1T′ MoS_2, which shows relatively low ΔG_{OH^*} value compared to Mn- and Cu-doped ones, respectively. Our calculations demonstrate that Co-, Ni-, and Cu-doped materials have the highest ΔG_{HO^*} values, which are also close to the desired value of −0.3 eV. As a result, Co-, Ni- and Cu-doped 1T′ MoS_2 are promising electrocatalysts

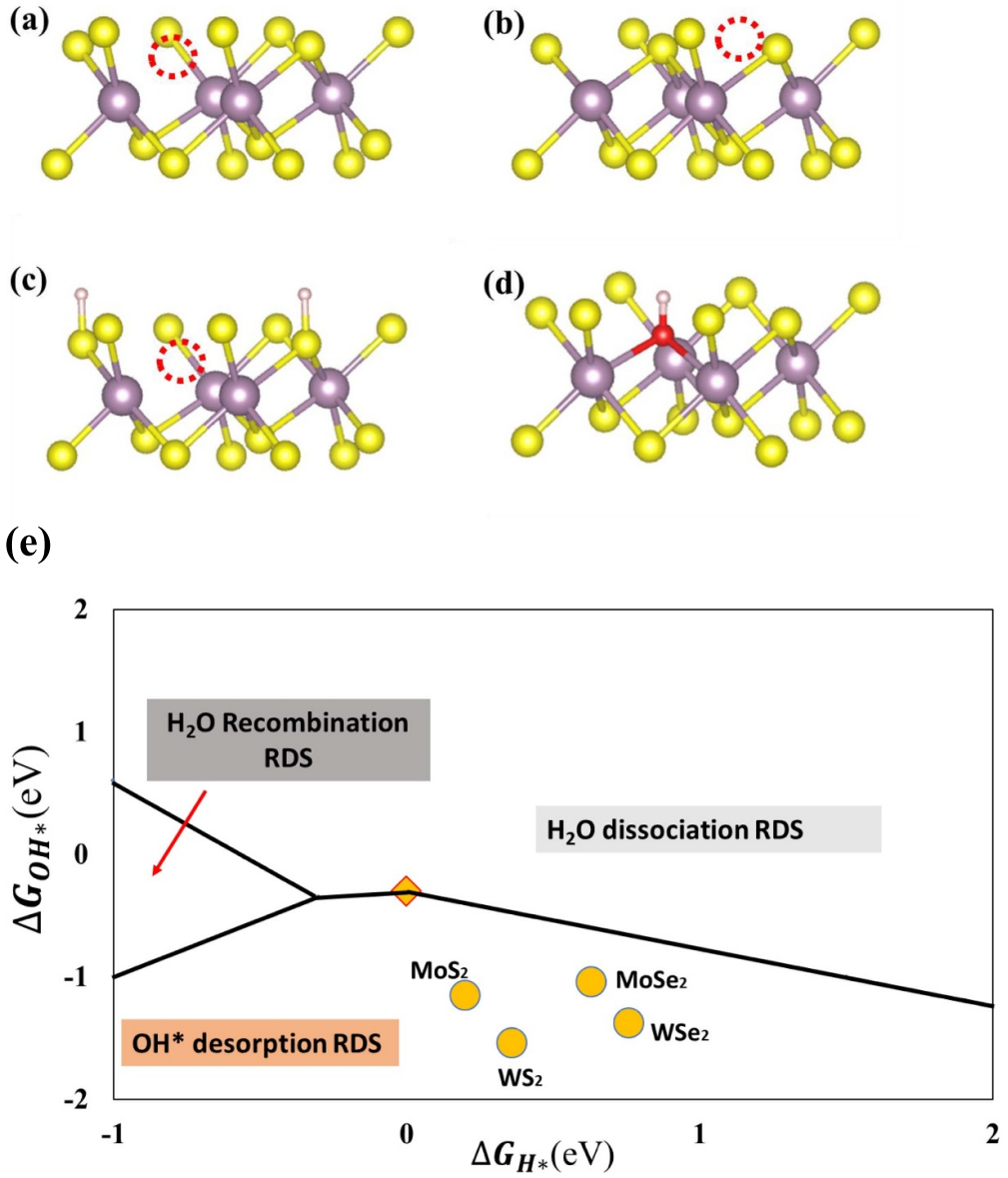

Figure 2. (a) Defective 1T′ TMD with one Low *X* vacancy; (b) defective 1T′ TMD with one High *X* vacancy; (c) defective 1T′ TMD with one Low *X* vacancy with H bonded on Low *X* site; (d) defective 1T′ TMD with OH adsorbed at Low *X* vacancy site; and (e) Volcano plot of ΔG_{HO^*} against ΔG_{H^*} of four TMDs with single *X* vacancy. Color code: yellow: *X* (S, Se), and purple: TM (Mo, W).

for alkaline HER. Indeed, the recent experiments have demonstrated that the Ni- and Co-doped 1T′ MoS_2 possess low overpotentials of -145 mV and -160 mV at a current density of 10 mA cm^{-2}, respectively, for alkaline HER [49], which validates our theoretical results. Our results further demonstrate that the combination of the Co and Ni dopants with the S vacancy may be the origin of the high performance toward alkaline HER [49–52]. Furthermore, our DFT results predict that the Cu-doped 1T′ defective MoS_2 may have the best alkaline HER performance, where ΔG_{OH^*} and ΔG_{H^*} are -0.22 and -0.06 eV, respectively.

Compared with the undoped defective MoS_2, the ΔG_{OH^*} values of these promising electrocatalysts significantly increase, indicating a reduction in their activity after doping. To better understand the impact of the TM dopants to deliver promising HER catalysts, the charge density difference of Cu-doped defective MoS_2 with the adsorbed OH species was calculated (see figure 4). For the sake of comparison, the charge density difference of the undoped defective MoS_2 with adsorbed OH species is also shown in figure 4. On the undoped defective 1T′ MoS_2, a large amount of charge densities are accumulated on the adsorbed OH. Accordingly, the charge densities of neighboring Mo atoms are depleted. The substantial charge transfer agrees with the low ΔG_{HO^*} value of the defective 1T′ MoS_2 shown in figure 2(e). As a result, the desorption of OH becomes the RDS during the alkaline HER. In contrast, the Cu-doped MoS_2 exhibits almost no charge density depletion on the Cu dopant. A small charge density accumulation between OH and Cu dopant is also observed. This supports that a weaker interaction between Cu and OH

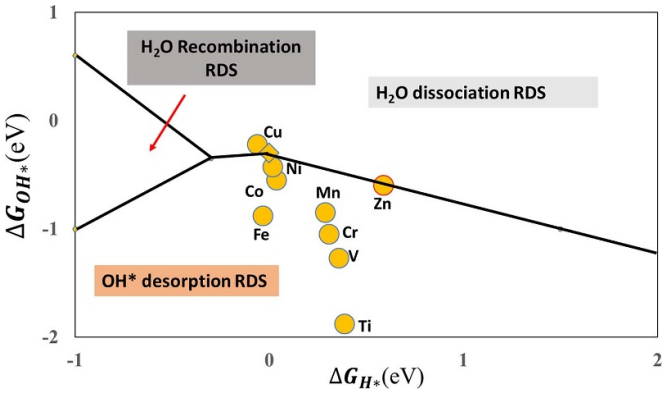

Figure 3. Volcano plot of ΔG_{OH^*} against ΔG_{H^*} using the 3d TMs doped single MoS_2 with single S vacancy.

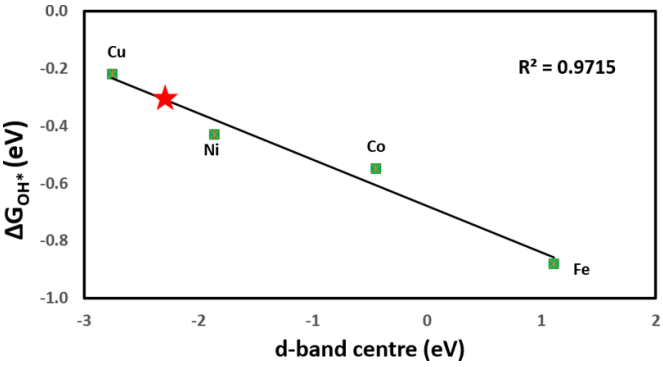

Figure 5. The relationship between the d-band center of 3d transition metals and their G_{OH^*} on 1T′ single S vacancy defective MoS_2.

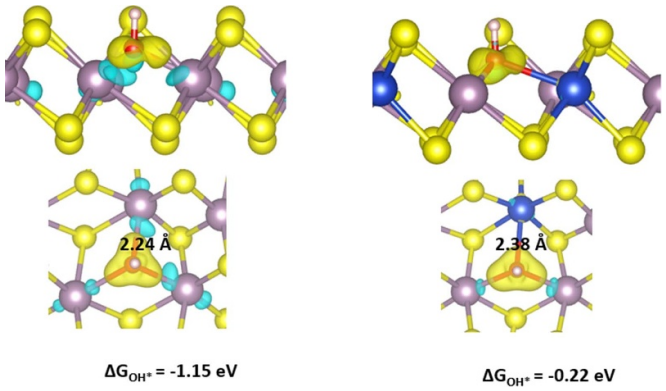

Figure 4. Charge density difference of pristine MoS_2 and Cu-doped MoS_2 with the adsorbed OH species: top: side view; bottom: top view. The iso-surface value is 0.01. Blue iso-surface: charge density depletion; yellow iso-surface: charge density accumulation.

species leads to the observed higher ΔG_{OH^*} value, which is beneficial to the desorption of adsorbed OH species and further enhances the alkaline HER performance.

The Fe-, Co-, Ni-, and Cu-doped 1T′ defective MoS_2 monolayers have different ΔG_{OH^*} values from -0.88 eV to -0.22 eV. This is expected due to the direct interaction between OH and the metal dopants. To understand the trend of the ΔG_{OH^*} values of Fe-, Co-, Ni-, Cu-doped 1T′ defective MoS_2 monolayers, the d-band center of the spin-down states of these dopants was calculated and listed in table S5. Figure 5 shows a direct correlation of d-band center energy with the free energy of OH adsorption to the surface of the doped catalyst. Our results indicate that the trend of this d-band center of the metals is positively correlated with the variance in the adsorption energies of OH intermediates on their doped 1T′ defective MoS_2. A reduced d-band center value from Fe to Cu suggests fewer vacant states, resulting in a higher Gibbs free energy change of OH adsorption. Hence, the shift of the d-band center can be used to explain the reactivity trend of these catalysts to OH adsorption.

Furthermore, the stability of the most promising Cu-doped defective MoS_2 was tested by *ab initio* molecular dynamics (AIMD) simulation within the Born–Oppenheimer schemes. Figure S1 shows the energy profile of Cu-doped defective MoS_2 over 3 ps at 300 K with the time step of 1 fs. The AIMD results demonstrate that the energies are well conserved over the time, which demonstrates that the system is thermodynamically stable after the introduction of Cu dopants and S vacancies.

4. Conclusion

In this study, we performed DFT calculations to explore MoS_2, WS_2, $MoSe_2$, and WSe_2-based electrocatalysts for alkaline HER applications. Different from the conventional methods for acidic HER electrocatalyst design, both ΔG_{OH^*} and ΔG_{H^*} were used as descriptors to evaluate the electrocatalytic performance. This is due to the importance of OH adsorption during water splitting in alkaline solution. Our findings indicated that MoS_2 performed best among the four pristine TMDs. However, the pristine TMDs show low reactivity in the adsorption of OH species. As a result, the water dissociation becomes the RDS. Defect engineering strategies, such as introducing single *X* vacancies, were further investigated to enhance their HER reactivity. However, the defective TMDs with single *X* vacancies show high reactivity to the adsorption of OH species. Consequently, the adsorbed OH species can efficiently desorb from the vacancy site. To improve the performance of the catalysts, the 3d metal dopants were theoretically screened in the 1T′ defective MoS_2. Among all the systems investigated, Cu-doped MoS_2 with one S vacancy emerged as the most promising electrocatalyst for HER in alkaline media. The electronic property analysis revealed that the superior performance of Cu-doped defective MoS_2 can be attributed to the suitable d-band center of Cu cations, which greatly reduces the activity of active sites to achieve the desired OH and H adsorption strengths. This reduced reactivity was further confirmed through the charge density difference analysis. These

findings provide insights into the potential of defective TMDs as catalysts for alkaline HER and highlight the importance of defect engineering strategies for further improvement.

Data availability statement

All data that support the findings of this study are included within the article (and any supplementary files).

Acknowledgments

The authors acknowledge financial support from the Australian Research Council Discovery Project (Grant No. DP210103266). This research was undertaken on the supercomputers in National Computational Infrastructure in Canberra, Australia, which the Australian Commonwealth Government and Pawsey Supercomputing Centre in Perth with funding from the Australian government and the Government of Western Australia support. Calculations were performed using resources from Grand Equipement National de Calcul Intensif (Grant No. A0120913426). Computational resources provided by the computing facilities Mésocentre de Calcul Intensif Aquitain of the Université de Bordeaux and the Université de Pau et des Pays de l'Adour. We acknowledge funding from the CNRS Institute of Chemistry through the 'International Emerging Actions 2022' mobility grant (2DH2 project) and from Agence national de recherche under the PIXIES ANR project (Grant Number ANR-22-CE08-0014).

Conflict of interest

The authors declare no conflict of interest.

ORCID iDs

Assil Bouzid https://orcid.org/0000-0002-9363-7240
Jack Jon Hinsch https://orcid.org/0000-0001-6897-4395
Jessica Jein White https://orcid.org/0000-0003-3635-3572
Yun Wang https://orcid.org/0000-0001-8619-0455

References

[1] Odenweller A, Ueckerdt F, Nemet G, Jensterle M and Luderer G 2022 Probabilistic feasibility space of scaling up green hydrogen supply *Nat. Energy* **7** 854–65
[2] Yu Z Y, Duan Y, Feng X Y, Yu X X, Gao M R and Yu S H 2021 Clean and affordable hydrogen fuel from alkaline water splitting: past, recent progress, and future prospects *Adv. Mater.* **33** 2007100
[3] Shi Y and Zhang B 2016 Recent advances in transition metal phosphide nanomaterials: synthesis and applications in hydrogen evolution reaction *Chem. Soc. Rev.* **45** 1529–41
[4] Pan Y, Sun K, Lin Y, Cao X, Cheng Y, Liu S, Zeng L, Cheong W-C, Zhao D and Wu K 2019 Electronic structure and d-band center control engineering over M-doped CoP (M = Ni, Mn, Fe) hollow polyhedron frames for boosting hydrogen production *Nano Energy* **56** 411–9
[5] Ďurovič M, Hnát J and Bouzek K 2021 Electrocatalysts for the hydrogen evolution reaction in alkaline and neutral media. A comparative review *J. Power Sources* **493** 229708
[6] Lin L, Sherrell P, Liu Y, Lei W, Zhang S, Zhang H, Wallace G G and Chen J 2020 Engineered 2D transition metal dichalcogenides—a vision of viable hydrogen evolution reaction catalysis *Adv. Energy Mater.* **10** 1903870
[7] Choi S, Kwon K C, Kim S Y and Jang H W 2017 Tailoring catalytic activities of transition metal disulfides for water splitting *FlatChem* **4** 68–80
[8] Yang J, Mohmad A R, Wang Y, Fullon R, Song X, Zhao F, Bozkurt I, Augustin M, Santos E J and Shin H S 2019 Ultrahigh-current-density niobium disulfide catalysts for hydrogen evolution *Nat. Mater.* **18** 1309–14
[9] Zhao X, Ma X, Sun J, Li D and Yang X 2016 Enhanced catalytic activities of surfactant-assisted exfoliated WS_2 nanodots for hydrogen evolution *ACS Nano* **10** 2159–66
[10] Lu Q P, Yu Y F, Ma Q L, Chen B and Zhang H 2016 2D transition-metal-dichalcogenide-nanosheet-based composites for photocatalytic and electrocatalytic hydrogen evolution reactions *Adv. Mater.* **28** 1917–33
[11] Lv R T, Robinson J A, Schaak R E, Sun D, Sun Y F, Mallouk T E and Terrones M 2015 Transition metal dichalcogenides and beyond: synthesis, properties, and applications of single- and few-layer nanosheets *Acc. Chem. Res.* **48** 56–64
[12] Geng X, Sun W, Wu W, Chen B, Al-Hilo A, Benamara M, Zhu H, Watanabe F, Cui J and Chen T-P 2016 Pure and stable metallic phase molybdenum disulfide nanosheets for hydrogen evolution reaction *Nat. Commun.* **7** 10672
[13] Lukowski M A, Daniel A S, Meng F, Forticaux A, Li L and Jin S 2013 Enhanced hydrogen evolution catalysis from chemically exfoliated metallic MoS_2 nanosheets *J. Am. Chem. Soc.* **135** 10274–7
[14] Qi Y H, Xu Q, Wang Y, Yan B, Ren Y M and Chen Z M 2016 CO_2-induced phase engineering: protocol for enhanced photoelectrocatalytic performance of 2D MoS_2 nanosheets *Acs Nano* **10** 2903–9
[15] Tan C L *et al* 2018 Preparation of high-percentage 1T-phase transition metal dichalcogenide nanodots for electrochemical hydrogen evolution *Adv. Mater.* **30** 1705509
[16] Lai Z C *et al* 2018 Preparation of 1T′-Phase $ReS_{2x}Se_{2(1-x)}$ (x = 0−1) nanodots for highly efficient electrocatalytic hydrogen evolution reaction *J. Am. Chem. Soc.* **140** 8563–8
[17] Tang Q and Jiang D-E 2016 Mechanism of hydrogen evolution reaction on 1T-MoS_2 from first principles *ACS Catal.* **6** 4953–61
[18] Wu L and Hofmann J P 2021 Comparing the intrinsic HER activity of transition metal dichalcogenides: pitfalls and suggestions *ACS Energy Lett.* **6** 2619–25
[19] Prabhu P, Jose V and Lee J-M 2020 Design strategies for development of TMD-based heterostructures in electrochemical energy systems *Matter* **2** 526–53
[20] Sheng W, Zhuang Z, Gao M, Zheng J, Chen J G and Yan Y 2015 Correlating hydrogen oxidation and evolution activity on platinum at different pH with measured hydrogen binding energy *Nat. Commun.* **6** 5848
[21] McCrum I T and Koper M T 2020 The role of adsorbed hydroxide in hydrogen evolution reaction kinetics on modified platinum *Nat. Energy* **5** 891–9
[22] Dong Y, Dang J, Wang W, Yin S and Wang Y 2018 First-principles determination of active sites of Ni metal-based electrocatalysts for hydrogen evolution reaction *ACS Appl. Mater. Interfaces* **10** 39624–30
[23] Perdew J P, Burke K and Ernzerhof M 1996 Generalized gradient approximation made simple *Phys. Rev. Lett.* **77** 3865–8
[24] Blochl P E 1994 Projector augmented-wave method *Phys. Rev.* B **50** 17953

[25] Dubbeldam D, Vreede J, Vlugt T J and Calero S 2019 Highlights of (bio-) chemical tools and visualization software for computational science *Curr. Opin Chem. Eng.* **23** 1–13
[26] Skúlason E, Tripkovic V, Björketun M E, Gudmundsdóttir S, Karlberg G, Rossmeisl J, Bligaard T, Jónsson H and Nørskov J K 2010 Modeling the electrochemical hydrogen oxidation and evolution reactions on the basis of density functional theory calculations *J. Phys. Chem.* C **114** 18182–97
[27] Wang V, Xu N, Liu J C, Tang G and Geng W T 2021 VASPKIT: a user-friendly interface facilitating high-throughput computing and analysis using VASP code *Comput. Phys. Commun.* **267** 108033
[28] Grimme S, Antony J, Ehrlich S and Krieg H 2010 A consistent and accurate *ab initio* parametrization of density functional dispersion correction (DFT-D) for the 94 elements H-Pu *J. Chem. Phys.* **132** 154104
[29] Liu J, Hinsch J J, Yin H, Liu P, Zhao H and Wang Y 2022 Low-dimensional metal–organic frameworks with high activity and selectivity toward electrocatalytic chlorine evolution reactions *J. Phys. Chem.* C **126** 7066–75
[30] Wang Y, Liu X, Liu J X, Al-Mamun M, Liew A W C, Yin H J, Wen W, Zhong Y L, Liu P R and Zhao H J 2018 Electrolyte effect on electrocatalytic hydrogen evolution performance of one-dimensional cobalt-dithiolene metal-organic frameworks: a theoretical perspective *ACS Appl. Energy Mater.* **1** 1688–94
[31] Liu J X, Kang J and Wang Y 2019 Molecular discovery of half-metallic one-dimensional metal-organic framework *J. Appl. Phys.* **125** 142906
[32] Liu J X, Yin H J, Liu P R, Chen S, Yin S W, Wang W L, Zhao H J and Wang Y 2019 Theoretical understanding of electrocatalytic hydrogen production performance by low-dimensional metal-organic frameworks on the basis of resonant charge-transfer mechanisms *J. Phys. Chem. Lett.* **10** 6955–61
[33] Zhu J, Hu L, Zhao P, Lee L S and Wong K-Y 2020 Recent advances in electrocatalytic hydrogen evolution using nanoparticles *Chem. Rev.* **120** 851–918
[34] Yin X, Tang C S, Zheng Y, Gao J, Wu J, Zhang H, Chhowalla M, Chen W and Wee A T 2021 Recent developments in 2D transition metal dichalcogenides: phase transition and applications of the (quasi-) metallic phases *Chem. Soc. Rev.* **50** 10087–115
[35] Putungan D B, Lin S-H and Kuo J-L 2015 A first-principles examination of conducting monolayer 1T′-MX_2 (M = Mo, W; X = S, Se, Te): promising catalysts for hydrogen evolution reaction and its enhancement by strain *Phys. Chem. Chem. Phys.* **17** 21702–8
[36] Liu Z, Li N, Su C, Zhao H, Xu L, Yin Z, Li J and Du Y 2018 Colloidal synthesis of 1T' phase dominated WS_2 towards endurable electrocatalysis *Nano Energy* **50** 176–81
[37] Yu Y, Nam G-H, He Q, Wu X-J, Zhang K, Yang Z, Chen J, Ma Q, Zhao M and Liu Z 2018 High phase-purity 1T′-MoS_2-and 1T′-$MoSe_2$-layered crystals *Nat. Chem.* **10** 638–43
[38] Huang W and Li W-X 2019 Surface and interface design for heterogeneous catalysis *Phys. Chem. Chem. Phys.* **21** 523–36
[39] Ambrosi A, Sofer Z and Pumera M 2015 2H→1T phase transition and hydrogen evolution activity of MoS_2, $MoSe_2$, WS_2 and WSe_2 strongly depends on the MX_2 composition *Chem. Commun.* **51** 8450–3
[40] Chia X and Pumera M 2018 Layered transition metal dichalcogenide electrochemistry: journey across the periodic table *Chem. Soc. Rev.* **47** 5602–13
[41] Kazemi S A, Yengejeh S I, Wang V, Wen W and Wang Y 2022 Theoretical understanding of electronic and mechanical properties of 1T′ transition metal dichalcogenide crystals *Beilstein J. Nanotech.* **13** 160–71
[42] Yengejeh S I, Liu J X, Kazemi S A, Wen W and Wang Y 2020 Effect of structural phases on mechanical properties of molybdenum disulfide *Acs Omega* **5** 5994–6002
[43] Kazemi S A, Yengejeh S I, Ogunkunle S A, Zhang L, Wen W, Liew AWC and Wang Y 2023 Vacancy impacts on electronic and mechanical properties of MX_2 (M = Mo, W and X = S, Se) monolayers *RSC Adv.* **13** 6498–506
[44] Zhang S, Wang C G, Li M Y, Huang D, Li L J, Ji W and Wu S W 2017 Defect structure of localized excitons in a WSe_2 monolayer *Phys. Rev. Lett.* **119** 046101
[45] Hus S M, Ge R J, Chen P A, Liang L B, Donnelly G E, Ko W, Huang F M, Chiang M H, Li A P and Akinwande D 2021 Observation of single-defect memristor in an MoS_2 atomic sheet *Nat. Nanotechnol.* **16** 58–62
[46] Lin Y C *et al* 2015 Three-fold rotational defects in two-dimensional transition metal dichalcogenides *Nat. Commun.* **6** 6736
[47] Zhou W, Zou X, Najmaei S, Liu Z, Shi Y, Kong J, Lou J, Ajayan P M, Yakobson B I and Idrobo J-C 2013 Intrinsic structural defects in monolayer molybdenum disulfide *Nano Lett.* **13** 2615–22
[48] Ippolito S and Samorì P 2022 Defect engineering strategies toward controlled functionalization of solution-processed transition metal dichalcogenides *Small Sci.* **2** 2100122
[49] Attanayake N H, Dheer L, Thenuwara A C, Abeyweera S C, Collins C, Waghmare U V and Strongin D R 2020 Ni- and Co-substituted metallic $MoS_{(2)}$ for the alkaline hydrogen evolution reaction *ChemElectroChem* **7** 3606–15
[50] Deng J, Li H, Xiao J, Tu Y, Deng D, Yang H, Tian H, Li J, Ren P and Bao X 2015 Triggering the electrocatalytic hydrogen evolution activity of the inert two-dimensional MoS_2 surface via single-atom metal doping *Energy Environ. Sci.* **8** 1594–601
[51] Wang H, Tsai C, Kong D, Chan K, Abild-Pedersen F, Nørskov J K and Cui Y 2015 Transition-metal doped edge sites in vertically aligned MoS_2 catalysts for enhanced hydrogen evolution *Nano Res.* **8** 566–75
[52] Venkatesh P S, Kannan N, Babu M G, Paulraj G and Jeganathan K 2022 Transition metal doped MoS_2 nanosheets for electrocatalytic hydrogen evolution reaction *Int. J. Hydrog. Energy* **47** 37256–63